AGU PUBLICATIONS

JGR

Journal of Geophysical Research: Atmospheres

RESEARCH ARTICLE

10.1002/2016JD025955

Key Points:

- Consistent with the moisture model theory, the moist static energy (MSE) can be used as a good proxy for MJO convection
- The vertically integrated horizontal MSE advection plays a critical role for eastward propagation of the MJO
- Faithful representation of seasonal mean MSE and MJO winds in the lower troposphere is key for realistic simulations of MJO propagation

Correspondence to:
X. Jiang,
xianan@ucla.edu

Citation:
Jiang, X. (2017), Key processes for the eastward propagation of the Madden-Julian Oscillation based on multimodel simulations, *J. Geophys. Res. Atmos.*, *122*, 755–770, doi:10.1002/2016JD025955.

Received 18 SEP 2016
Accepted 10 JAN 2017
Accepted article online 11 JAN 2017
Published online 24 JAN 2017

Key processes for the eastward propagation of the Madden-Julian Oscillation based on multimodel simulations

Xianan Jiang[1,2]

[1]Joint Institute for Regional Earth System Science and Engineering, University of California, Los Angeles, California, USA, [2]Jet Propulsion Laboratory, California Institute of Technology, Pasadena, California, USA

Abstract As a prominent climate variability mode with widespread influences on global weather extremes, the Madden-Julian Oscillation (MJO) remains poorly represented in the latest generation of general circulation models (GCMs), with a particular challenge in simulating its eastward propagating convective signals. In this study, by analyzing multimodel simulations from a recent global MJO model evaluation project, an effort is made to identify key processes for the eastward propagation of the MJO through analyses of moisture entropy (ME) processes under a "moisture mode" framework for the MJO. The column-integrated horizontal ME advection is found to play a critical role for the eastward propagation of the MJO in both observations and good MJO models, with a primary contribution through advection of the lower tropospheric seasonal mean ME by the MJO anomalous circulations. By contrast, the horizontal ME advection effect for the eastward propagation is greatly underestimated in poor MJO GCMs, due to model deficiencies in simulating both the seasonal mean ME pattern and MJO circulations, leading to a largely stationary MJO mode in these GCMs. These results thus pinpoint an important guidance toward improved representation of the MJO in climate and weather forecast models. While this study mainly focuses on fundamental physics for the MJO propagation over the Indian Ocean, complex influences by the Maritime Continent on the MJO and also ME processes associated with the MJO over the western Pacific warrant further investigations.

1. Introduction

As a dominant intraseasonal variability mode of tropical atmosphere, the Madden-Julian Oscillation (MJO) [*Madden and Julian*, 1971, 1972] not only exerts widespread influences on global weather extremes in both tropics and extratropics but also plays an active role in shaping the lower frequency variability (e.g., El Nino–Southern Oscillation) and the climate state of the global atmosphere-ocean system (see reviews by *Zhang* [2005], *Lau and Waliser* [2012], *Zhang* [2013], and *Serra et al.* [2014]). Meanwhile, serving as one of primary predictability sources for extended-range weather prediction [*Waliser*, 2012; *Neena et al.*, 2014], the MJO has been recognized for its significant impacts on climate predictions and projections [*National Academies Press*, 2010, 2016; *Vitart et al.*, 2012]. Moreover, the MJO is considered a key element for the recently advocated "seamless prediction" concept [e.g., *Hurrell et al.*, 2009; *Brown et al.*, 2012; *Hoskins*, 2013].

However, the MJO remains poorly represented in the latest generation of climate and weather forecast models [e.g., *Hung et al.*, 2013; *Jiang et al.*, 2015], with common model biases including too weak amplitude and lack of systematic eastward propagation. While model deficiencies in depicting cumulus processes are generally blamed to be responsible for model inability to represent the MJO, essential MJO physics and key model processes for its realistic simulations are still elusive. Motivated by a longstanding and urgent need to improve the MJO in current weather forecasting and climate models, the MJO has been a central focus of several recent international projects in the tropical climate research community [*Zhang et al.*, 2013], including the Intraseasonal Variability Hindcast Experiment [*Neena et al.*, 2014; *Lee et al.*, 2015], the Year of Tropical Convection (YOTC) virtual field campaign [*Moncrieff et al.*, 2012; *Waliser et al.*, 2012], the Cooperative Indian Ocean Experiment on Intraseasonal Variability (CINDY2011) and Dynamics of the MJO [*Yoneyama et al.*, 2013], and the project on Subseasonal to Seasonal Prediction [*Vitart et al.*, 2012].

Particularly, a global model intercomparison project, with a specific focus on the vertical structure and physical processes of the MJO, was recently organized by the YOTC MJO Task Force (MJOTF) and the Global Energy and Water Cycle Experiment Atmospheric System Study (GASS) program [*Petch et al.*, 2011; *Jiang et al.*, 2015; *Klingaman et al.*, 2015a]. More than 30 general circulation models (GCMs) participated in this multimodel evaluation project by addressing at least one of the three experimental components of this project, i.e., a 20 year climate simulation component [*Jiang et al.*, 2015] and two hindcast components [*Xavier et al.*, 2015; *Klingaman et al.*, 2015b]. By analyzing GCMs that participated in the climate simulation component, *Jiang et al.* [2015] has shown that the systematic eastward propagation of the MJO is only relatively well simulated in about one fourth of the total 27 models, while a majority of these models exhibit a stationary or even westward propagating intraseasonal mode. In attempting to discriminate key processes for realistic MJO simulations, two process-oriented metrics, i.e., the low-level relative humidity difference between high and low rain events and seasonal mean gross moist stability, exhibit moderate correlations with the model skill for MJO propagation [*Jiang et al.*, 2015]. Nevertheless, critical model processes for realistic simulations of the MJO in climate models still need to be identified.

This study is an extension of the work by *Jiang et al.* [2015]. Built upon the "moisture mode" framework previously proposed for the MJO study [e.g., *Yu and Neelin*, 1994; *Raymond and Fuchs*, 2009; *Sobel and Maloney*, 2013; *Adames and Kim*, 2016], key model physics responsible for the eastward propagation of the MJO is explored in this study by analyzing moist static energy (MSE) processes in multimodel simulations, particularly by comparing these processes between two model groups, i.e., good versus poor GCMs in representing the eastward propagation of the MJO. The structure of this manuscript is as follows. Details of model output from GCMs participating in the climate simulation component of the MJOTF/GASS MJO model comparison project along with observational data set used for this study are provided in section 2. Section 3 describes methods to extract MSE terms associated with the MJO based on both observations and model simulations. Justification of the approach based on MSE diagnosis for understanding propagation of MJO convective signals, and main results on key processes for the eastward propagation of the MJO obtained from these multimodel simulations, are presented in section 4. Finally, a summary of main findings from this study and a brief discussion will be presented in section 5.

2. Data Sets

2.1. Climate Model Simulation Data Set

Table 1 lists names of 24 GCMs analyzed in this study, participating in the climate simulation component of the MJOTF/GASS MJO project, along with their horizontal and vertical resolutions. All these participating models, either with an atmospheric-only GCM (AGCM) or an atmosphere-ocean coupled system, were integrated for 20 years. For AGCM runs, weekly sea surface temperatures and sea ice concentrations based on the NOAA Optimum Interpolation V2 product [*Reynolds et al.*, 2002] for the 20 year period of 1991–2010 were specified as the model lower boundary conditions. Output from all the participating GCMs was archived at every 6 h on standard horizontal (2.5° × 2.5°) grids and 22 vertical pressure levels. Variables analyzed in this study include 3-D winds, temperature, specific humidity, radiative heating, and also 2-D fields including rainfall and surface heat flux terms. More details of the MJOTF/GASS MJO model comparison project, and access to these multimodel output, can be found in the project website: http://www.ucar.edu/yotc/mjodiab.html.

2.2. Observations

The primary observational data sets used for this analysis include Tropical Rainfall Measuring Mission (TRMM)-based rainfall observations (version 3B42 v7) [*Huffman et al.*, 2007] and the European Centre for Medium-Range Weather Forecasts ERA-Interim reanalysis [*Dee et al.*, 2011] for the period of 1998–2012. TRMM 3B42 rainfall provides precipitation estimates with 3-hourly temporal resolution on a 0.25° spatial resolution in a global belt extending from 50°S to 50°N. With a horizontal resolution of 1.5° × 1.5°, the ERA-Interim reanalysis provides daily 3-D profiles of temperature, specific humidity, *u* and *v* winds, pressure vertical velocity, and 2-D surface heat fluxes, required for calculating MSE terms. Both the raw TRMM rainfall and ERA-Interim reanalysis data are interpolated onto the same grids as the GCM output, i.e., 2.5° × 2.5° at 22 standard vertical pressure levels.

Meanwhile, daily 3-D fields of TRMM-based estimate of radiative heating based on the Hydrologic Cycle and Earth's Radiation Budget algorithm [*L'Ecuyer and McGarragh*, 2010] is used to examine radiative effects on MJO propagation. While some amount of uncertainty exists with this satellite-retrieved radiative heating data set, it provides valuable additions to the reanalysis and has been previously used to characterize the vertical heating structure of the MJO [*Jiang et al.*, 2011].

Table 1. Models With Horizontal/Vertical Resolutions Analyzed in This Study

	Model Name	Institute	Hori. Resolution (lon × lat), Vertical Levels
1	ACCESS1	*Centre for Australian Weather and Climate Research*	1.875° × 1.25° , L85
2	BCC-AGCM2.1	*Beijing Climate Center, China Meteorological Administration*	T42 (2.8), L26
3	CAM5	*National Center for Atmospheric Research*	1.25° × 0.9°, L30
4	CAM5-ZM	*Lawrence Livermore National Laboratory*	1.25° × 0.9°, L30
5	CanCM4	*Canadian Centre for Climate Modelling and Analysis*	2.8°, L35
6	CFS2	*Climate Prediction Center, National Centers for Environmental Prediction /NOAA*	T126 (1°), L64
7	CNRM-AM	*Centre National de la Recherche Scientifique/Météo-France*	T127 (1.4), L31
8	CNRM-CM		
9	CNRM-ACM		
10	CWB-GFS	*Central Weather Bureau, Taiwan*	T119 (1°), L40
11	ECEarth3	*Rossby Centre, Swedish Meteorological and Hydrological Institute*	T255 (80 km), L91
12	EC-GEM	*Environment Canada*	1.4°, L64
13	ECHAM6	*Max Planck Institute for Meteorology*	T63 (2°), L47
14	FGOALS-s2	*Institute of Atmospheric Physics, Chinese Academy of Sciences*	R42 (2.8° × 1.6°), L26
15	GEOS5	*Global Modeling and Assimilation Office, NASA*	0.625° × 0.5°, L72
16	GISS-E2	*Goddard Institute for Space Studies, NASA*	2.5° × 2.0°, L40
17	ISUGCM	*Iowa State University*	T42 (2.8°), L18
18	MIROC5	*Atmosphere and Ocean Research Institute/National Institute for Environmental Studies/Japan Agency for Marine-Earth Science and Technology, Japan*	T85 (1.5°), L40
19	MRI-AGCM3	*Meteorological Research Institute, Japan*	T159, L48
20	NavGEM1	*U.S. Naval Research Laboratory*	T359 (37 km), L42
21	SPCAM3	*Colorado State University*	T42 (2.8°), L30
22	SPCCSM3	*George Mason University*	T42 (2.8°), L30
23	TAMU-CAM4	*Texas A&M University*	2.5° × 1.9°, L26
24	UCSD-CAM3	*Scripps Institute of Oceanography*	T42 (2.8°), L26

3. Column Moist Static Energy Analysis for the MJO

Viewing the MJO from a moisture mode paradigm, the MSE equation has been widely used to understand MJO physics [e.g., *Maloney*, 2009; *Kiranmayi and Maloney*, 2011; *Andersen and Kuang*, 2012; *Sobel and Maloney*, 2012; *Kim et al.*, 2014; *Sobel et al.*, 2014; *Pritchard and Bretherton*, 2014; *Inoue and Back*, 2015; *Adames and Kim*, 2016; *Wolding et al.*, 2106]. The critical basis of the moisture mode framework for the MJO is that over the Indo-Pacific warm pool region, where the MJO exhibits the strongest amplitude, the fundamental physics of the MJO is regulated by atmospheric moisture under the weak temperature gradient condition [*Sobel et al.*, 2001; *Raymond*, 2001]. Also, as moisture effect dominates the column MSE, diagnosis of MSE processes thus provides critical insight into MJO physics.

In this study, an alternate form of the conventional MSE equation, namely, the moist entropy equation, is used following *Raymond et al.* [2009] and *Benedict et al.* [2014], which is valid for temperatures either above or below freezing [*Raymond*, 2013]. The specific moist entropy (s) is defined as follows,

$$s = (C_{PD} + r_V C_{PV})\ln(T/T_R) - R_D \ln(p_D/p_R) - r_V R_V \ln(p_V/e_{SF}) + L_V r_V/T_R \tag{1}$$

where C_{PD}, R_D, and p_D are the specific heat, gas constant, and partial pressure of dry air respectively, while C_{PV}, R_V, and p_V are the specific heat, gas constant, and partial pressure of water vapor; r_V is the water vapor mixing ratio; T is air temperature; T_R is the reference temperature of 273.15 K; $e_{SF} = 611$ Pa, and $L_V(T) = 2.5 \times 10^6$ J kg^{-1} is the enthalpy of vaporization.

The vertically integrated moist entropy (S) equation can then be written as

$$[\partial S/\partial t] = -\left[\vec{V}\cdot\nabla S\right] - [\omega(\partial S/\partial p)] + F_s + Q_R \tag{2}$$

where moist entropy (ME) $S = T_R \cdot s$, the square brackets represent mass-weighted vertical integrals from 1000 hPa to 100 hPa, $\vec{V}$ is the horizontal vector winds, ω is the vertical pressure velocity, F_s is total surface fluxes including sensible and latent heat fluxes, and Q_R is vertically integrated radiative (short-wave and long-wave) heat fluxes.

Since the systematic eastward propagation of the MJO is most pronounced over the Indian Ocean and western Pacific, to exclude complex influences on MJO propagation by the Maritime Continent, which is greatly difficult to be resolved in GCMs due to limited model resolution [*Neale and Slingo*, 2003; *Sato et al.*, 2009; *Hagos et al.*, 2016], in this study we confine our analyses to the Indian Ocean (IO) region. Also, analysis is

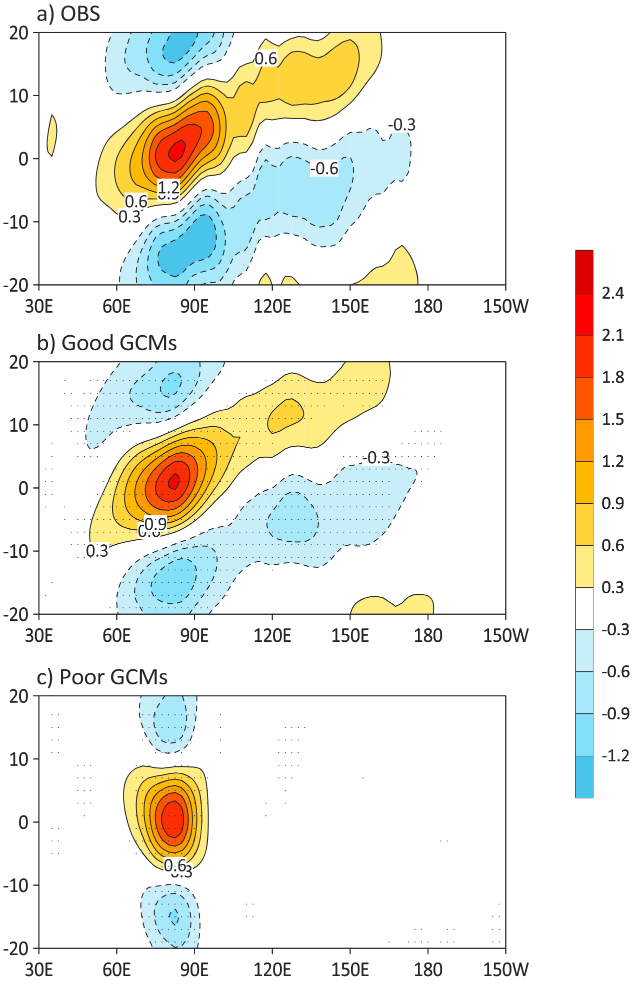

Figure 1. Longitude-time evolution of rainfall anomalies along the equator (10°S–10°N averaged; units: mm d^{-1}) in (a) observations, (b) composite of six good MJO GCMs, and (c) composite of six poor MJO GCMs, in capturing the eastward propagation of the MJO. All evolution patterns based on observations and models are derived by lag-regressions of 20–100 day band-pass-filtered anomalous rainfall against itself averaged over the equatorial Eastern Indian Ocean (75–85°E, 5°S–5°N) and normalized by a rainfall amplitude of 3 mm d^{-1} over the regression base point. Grid points where model composite rainfall anomalies are significant at 95% significance level are stippled.

limited to the boreal winter season from November to April to concentrate on fundamental model physics for the eastward propagation of the MJO. Spatial pattern of each vertically integrated ME budget term in equation (2), as well as anomalous rainfall and column ME fields associated with the MJO, is derived by regressing these fields onto a time series of 20–100 day band-pass-filtered rainfall averaged over the equatorial eastern IO (75–85°S, 5°S–5°N) for both observations and model simulations. Before conducting regressions, both rainfall and ME variables are subject to removal of the climatological annual cycle (annual mean plus three leading harmonics) and then a 20–100 day time filtering by applying a Lanczos band-pass time filter [*Duchon*, 1979]. With a particular focus on processes responsible for the MJO propagation rather than its amplitude, all the regressed patterns associated with the MJO in both observations and simulations are scaled by the same 3 mm d^{-1} rainfall anomaly at the IO base point for comparison purposes.

Meanwhile, a skill score for the eastward propagation of the MJO in each model is defined by pattern correlation of simulated rainfall Hovmöller diagram (time-longitude evolution) to the observational counterpart following *Jiang et al.* [2015]. The Hovmöller diagrams were constructed from lag-regressions (−20 to 20 days) of latitude-averaged (10°S–10°N), 20–100 day filtered precipitation onto a same base region over the IO (75°–85°E, 5°S–5°N). Two groups of GCMs are then identified, namely, good MJO GCMs for models with top 25% skill in capturing the eastward propagation of the MJO and poor MJO GCMs for models with bottom 25% skill. For detailed methods in defining model MJO propagation skill and identification of these good and poor MJO models, readers are referred to *Jiang et al.* [2015]. In this study, considering the availability of model output for ME analysis, good MJO models include six GCMs, i.e., CNRM-CM, GISS-E2, MRI-AGCM3, SPCAM3, SPCCSM3, and TAMU-CAM4, and six poor MJO GCMs include CanCM4, CWB-GFS, ISUGCM, MIROC5, NavGEM1, and UCSD-CAM3 (see Table 1 for details of these models).

4. Key Physics for MJO Propagation Based on Moist Entropy Analysis

4.1. Moist Entropy as a Proxy for MJO Convection

Figure 1 illustrates Hovmöller diagrams (longitude versus time in lag days) of rainfall anomalies along the equator based on lag-regressions against the IO base point for both TRMM, good and poor GCM composites. In agreement with the definition of good and poor MJO models, the observed eastward propagation of the MJO convection, with a phase speed of 5 ° d^{-1}, is well simulated in good GCM composite, while rainfall evolution in poor GCM composite exhibits a stationary or even a slightly westward propagating mode over the IO.

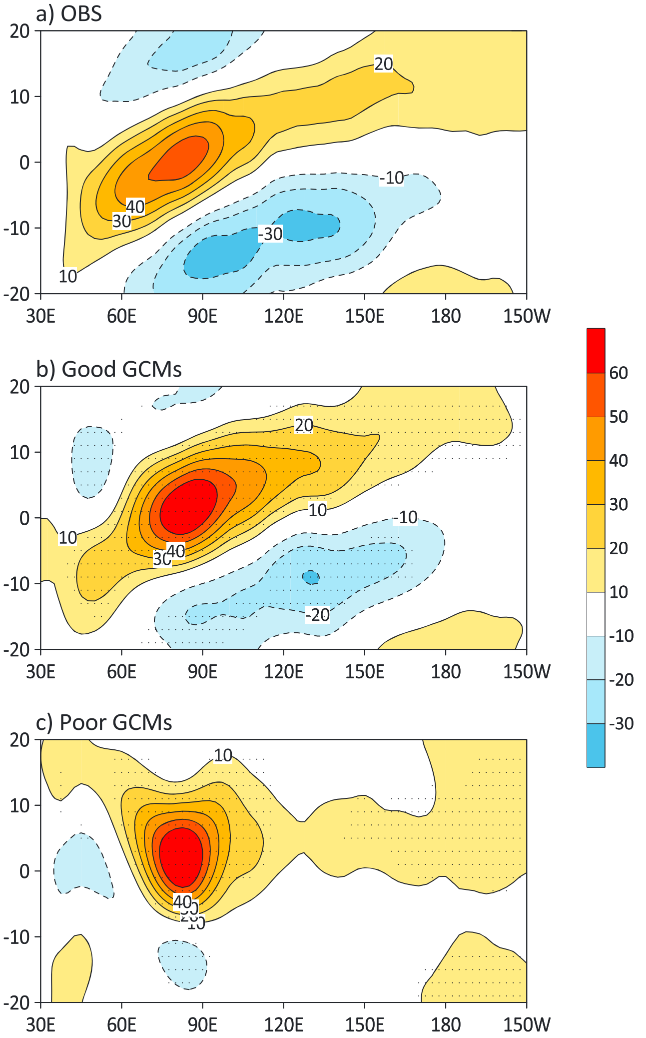

Figure 2. Same as in Figure 1 but for longitude-time evolution of ME anomalies (units: 10^{-5} J m^{-2}) in (a) observations, composites based on (b) good and (c) poor MJO models. Grid points where model composite ME anomalies are significant at 95% significance level are stippled.

As an initial validation of the moisture mode paradigm for the MJO, similar to rainfall anomalies in Figure 1, longitude-time evolution of column-integrated ME anomalies along the equator based on lag-regressions onto IO rainfall in observations and model composites for both good and poor MJO models are presented in Figure 2. Clearly evident is the systematic eastward propagation of ME anomalies in both observations and good MJO GCMs, in agreement with propagation of rainfall anomalies in Figure 1. Also consistent with rainfall evolution in poor GCMs (Figure 1c), regressed ME pattern is also characterized by a largely stationary or slightly westward propagating mode (Figure 2c). These results suggest that anomalous column ME can be used as a good proxy in depicting propagation of MJO convective signals, in accord with the aforementioned moisture mode theory for the MJO.

Figure 3 further illustrates spatial patterns of rainfall and column-integrated ME anomalies associated with the MJO in observations and good versus poor model composites, derived by lag-0 regressions of these fields onto rainfall anomalies over the IO box. Corresponding to enhanced MJO convection, the anomalous rainfall patterns in observations and model simulations are generally similar, albeit a relatively smaller size in convection organization is discernible in poor model composite (Figure 3c), which has also been noted in vertical profiles of vertical velocity and diabatic heating [*Jiang et al*., 2015, Figures 13 and 15], indicating plausible model deficiencies in representing convection organization in these poor MJO GCMs.

Corresponding anomalous column ME patterns associated with enhanced MJO convection over the IO are also illustrated in Figures 3d–3f. Positive ME anomalies are largely collocated with enhanced convection in both observations and two model composites. Noteworthy is the differences in amplitudes of ME anomalies in observations and model simulations, despite that all these regressed ME patterns are scaled by the same 3 mm d^{-1} rainfall at the regression base point over the IO. Different ME amplitudes in these model simulations are ascribed to different model convective moisture adjustment time scales, a measure of how rapidly precipitation must increase to remove excess column water vapor, or alternately the efficiency of surface precipitation generation per unit column water vapor anomaly [*Jiang et al*., 2016]. While convective adjustment time scale tends to be a model characteristic closely linked to model cumulus parameterization [*Jiang et al*., 2016], key model physics determining the convective adjustment time scale needs to be identified.

Spatial patterns of column ME tendency, derived by a similar lag-0 regression against the IO rainfall, are also shown in Figures 3g–3i for observations and good versus poor model composites. The observed ME tendency is characterized by a zonal dipole pattern (Figure 3g), with positive (negative) ME tendencies to the east (west) of ME center, in accord with the eastward propagation of ME and rainfall anomalies associated with the observed MJO. This east-west dipole pattern in ME tendency is well represented in good MJO models (Figure 3h) but not in poor models (Figure 3i). For the latter case, positive ME tendencies are evident over almost the entire tropical IO, with maximum positive values being slightly shifted to the west of convection center. These ME tendency patterns are consistent with strong eastward (weak westward) propagation of model MJO in good (poor) MJO GCMs.

Figure 4 further illustrates how model skill for the eastward propagation of the MJO is related to model fidelity in simulating the ME tendency pattern, measured by pattern correlation between each simulated and observed ME tendency pattern over the tropical IO (50–110°E, 10°S–10°N). As previously mentioned, model skill in representing the eastward propagation of MJO is based on pattern correlations of simulated rainfall Hovmöller diagrams to the observations following *Jiang et al*. [2015]. It is clearly suggested that models that better simulate the ME tendency pattern over the IO also exhibit higher skill in representing the eastward propagation of the MJO with a correlation of 0.75. Particularly, the six good MJO GCMs (red dots in Figure 4) that capture realistic eastward propagation of the MJO also show excellent skill in simulating ME tendency patterns. Meanwhile, the six poor MJO GCMs (blue dots in Figure 4) largely exhibit very low skill (close to 0 or negative pattern correlations) for ME tendency patterns.

These above results suggest that the most prominent features of MJO convection in the IO including its spatial pattern and evolution can be well depicted by column ME anomalies in both observations and simulations. Therefore, understanding of key processes responsible for the eastward propagation of ME anomalies associated with the MJO based on equation (2), particularly through comparison of processes between good and poor model simulations, will provide critical insights into essential model processes for realistic simulation of the eastward propagation of the MJO.

4.2. Key Processes for MJO Propagation Based on Moist Entropy Analysis

Spatial patterns of column-integrated ME budget terms associated with enhanced MJO convection over the IO, including horizontal and vertical ME advection, surface heat fluxes, and radiative heating based on both observations and model simulations, are displayed in Figure 5. Near the MJO center (about 80°E), both horizontal and vertical ME advection leads to negative ME tendencies, suggesting net ME export over MJO convectively active region in both observations and model simulations. For the horizontal ME advection patterns, the negative maxima are slightly westward displaced relative to convection center in both observations (Figure 5a) and good MJO models (Figure 5b), while the maximum center is more or less collocated with convection center in poor model simulations (Figure 5c). Meanwhile, positive ME tendencies by horizontal advection are detected on the eastern edge of MJO convection in observations and both good and poor GCM simulations. For the vertical ME advection, negative tendencies are dominant over the MJO convectively active region in observations (Figure 5d) and good MJO GCMs (Figure 5e). Due to smaller size of MJO convection in poor models as previously discussed (Figures 3c and 3f), positive ME tendencies are discerned over the western IO due to local descending motion (Figure 5f).

Meanwhile, positive ME tendencies by both Q_R and F_s are evident over regions with enhanced MJO convection in observations and both model composites, with their maximum centers slightly shifted to the west of MJO center particularly in the observations and good model composite. Further analysis indicates that total Q_R is dominated by long-wave radiative effect, and the westward shift of the maximum radiation-induced ME tendencies relative to convection center is mainly due to the backward vertical tilting structure in both anomalous cloud and moisture fields associated with the MJO (figures not shown [see *Tian et al*., 2010; *Jiang et al*., 2011, 2015]). The westward displacement in maximum ME tendency by F_s is mainly due to increased total surface wind speed to the west of convection given the westerly MJO anomalous winds superimposed on the weak seasonal mean surface westerlies over the equatorial IO (figures not shown). These results are consistent with previous studies on important roles of radiative effect and wind-evaporation feedback in energizing the MJO [e.g., *Raymond*, 2001; *Maloney and Sobel*, 2004; *Sobel et al*., 2008; *Andersen and Kuang*, 2012; *Jiang et al*., 2016]. Meanwhile, weak negative ME tendencies by both Q_R and F_s are noticeable to

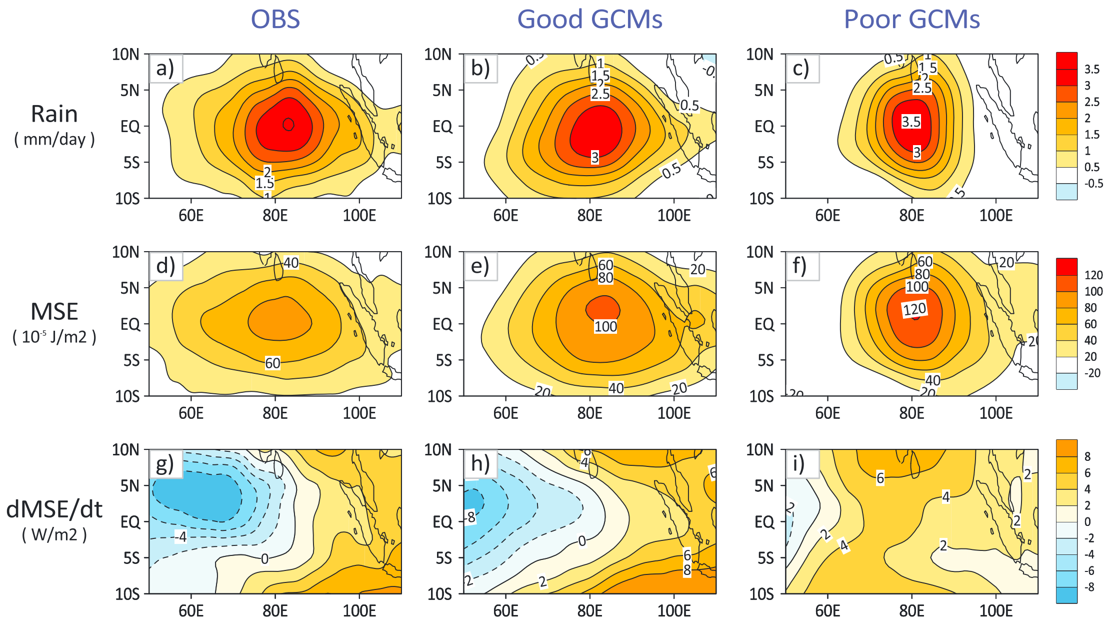

Figure 3. (a–c) Lag-0 regressed rainfall, (d–f) vertically integrated ME, and (g–i) ME tendency anomalies in observations (Figures 3a, 3d, and 3g), composites over good (Figures 3b, 3e, and 3h), and poor (Figures 3c, 3f, and 3i) MJO GCMs, scaled by the 3 mm d^{-1} rainfall averaged over the equatorial IO (75–85°E, 5°S–5°N).

the east of MJO convection in both observations and model simulations (Figures 5g–5l), indicating that ME tendencies induced by both Q_R and F_s tend to inhibit the eastward propagation of MJO convection.

Relative roles of different ME components on the right-hand side of equation (2) for the total ME tendency can then be objectively assessed by projecting the 2-D spatial pattern of each ME budget term in both observations and simulations onto the observed ME tendency pattern (i.e., Figure 3g). A positive projection coefficient for a particular ME term denotes its contribution for positive (negative) ME tendencies to the east (west) of convection center, thus leading to the eastward propagation of MJO convection as in the observations. On the contrary, a negative projection means that the specific process promotes the westward propagation of the convection. As previously mentioned, since we mainly focus on MJO propagation over the IO to exclude influences from the Maritime Continent, a domain of 50–110°E, 10°S–10°N is employed when performing these pattern projections. Another justification for adopting this projection domain is that the regressed ME patterns associated with the MJO are largely confined within this IO domain from day −1 to day +1 (figures not shown, see ME patterns at day 0 in Figure 3). Therefore, the ME tendency pattern at day 0 in this domain largely defines MJO propagation in the IO, as supported by the high correlation between model skill in simulating the ME tendency pattern at day 0 in this IO domain and skill for the MJO eastward propagation across model simulations (Figure 4).

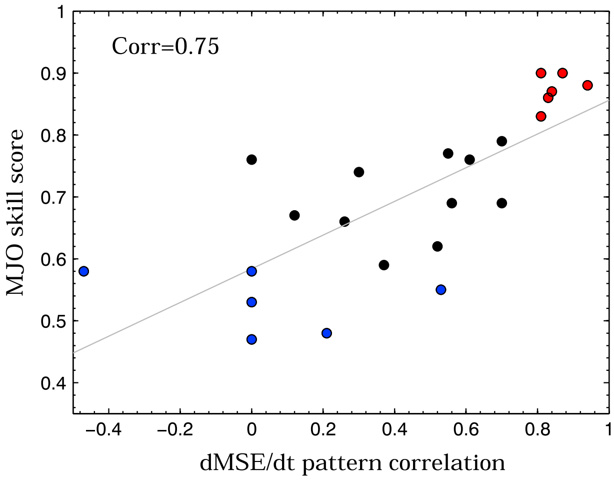

Figure 4. Scatterplot between MJO skill scores by pattern correlation of rainfall Hovmöller diagram in multimodel simulations (*y* axis) and model skill of ME tendency pattern (*x* axis) by pattern correlations between simulated and observed tendency patterns over the IO (50–110°E, 10°S–10°N).

Figure 6 displays pattern projection coefficients of each ME tendency term along with the total tendency in observations, good and poor model

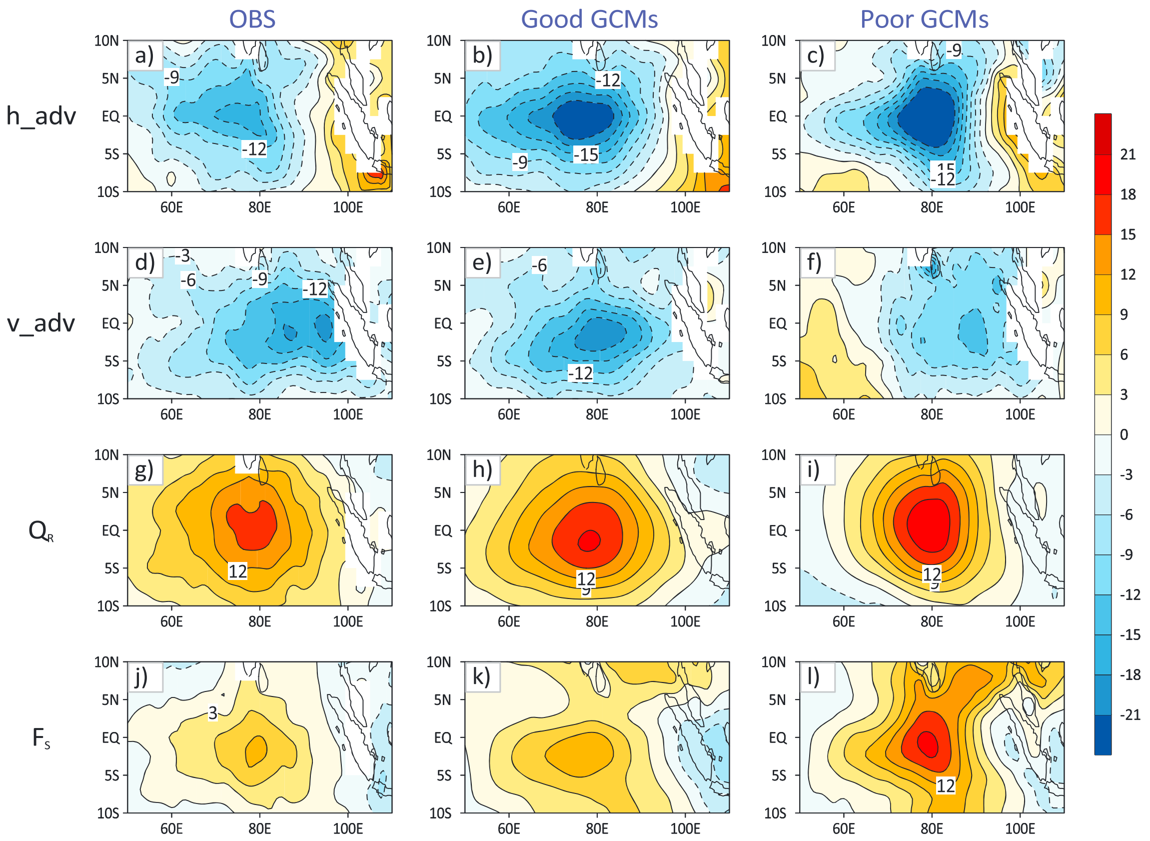

Figure 5. Lag-0 regressed patterns for vertically integrated ME tendency components, including (a–c) horizontal and (d–f) vertical ME advection, (g–i) radiative heating (long wave and short wave), and (j–l) surface fluxes (latent and sensible) in observations (Figures 5a, 5d, 5g, and 5j), composites over good (Figures 5b, 5e, 5h, and 5k), and poor (Figures 5c, 5f, 5i, and 5l) MJO models, corresponding to a 3 mm d^{-1} rainfall over the IO (75–85°E, 5°S–5°N). Units are W m^{-2} for all variables.

composites, respectively. In observations (Figure 6a), the projection of the total ME tendency onto itself is one by definition. The observed radiative processes (Q_R) and surface fluxes (F_s) tend to negatively contribute to the observed ME tendency in Figure 3g, largely due to the slightly westward displacement of their positive maxima relative to convection center and negative tendencies to the east of convection as previously discussed (Figures 5g and 5j), thus inhibiting the eastward propagation of MJO convection. Negative roles of radiative effects and surface fluxes for the observed eastward propagation of the MJO are consistent with previous studies [e.g., *Kiranmayi and Maloney*, 2011; *Andersen and Kuang*, 2012; *Sobel and Maloney*, 2013]. Also shown by Figure 6a, while the vertical ME advection plays a very minor role for the eastward propagation, the total observed ME tendency is largely ascribed to the horizontal ME advection. However, a significant positive ME budget residual is noted in the observations (Figure 6a), which was also previously reported [*Kiranmayi and Maloney*, 2011; *Kim et al.*, 2014]. In addition to the use of horizontally and vertically interpolated data rather than the original model data for the analysis and also the analysis increment in the reanalysis data [*Kiranmayi and Maloney*, 2011; *Mapes and Bacmeister*, 2012], the use of TRMM-based Q_R estimates could also lead to the large budget residual. Projections of ME tendency patterns from good MJO models to the observed ME tendency pattern give rise to generally similar results as in the observations (Figure 6b). The total ME tendency pattern in good model simulations exhibits a high projection to its observational counterpart, in agreement with the well-simulated total ME tendency pattern in good MJO models (cf. Figure 3h versus Figure 3g). Moreover, as in the observations, both Q_R and F_s negatively contribute to the eastward propagation in good MJO models. While vertical ME advection plays a minor role for the eastward propagation in good model simulations, the most dominant contributor to the total ME tendency is also from the horizontal ME advection.

By contrast, projection of the total ME tendency in poor model simulations yields a near-zero projection coefficient (Figure 6c), consistent with a largely stationary MJO mode in these models. Also in contrast to the observations and good model composite, in addition to tendencies by Q_R and F_s, vertical ME advection

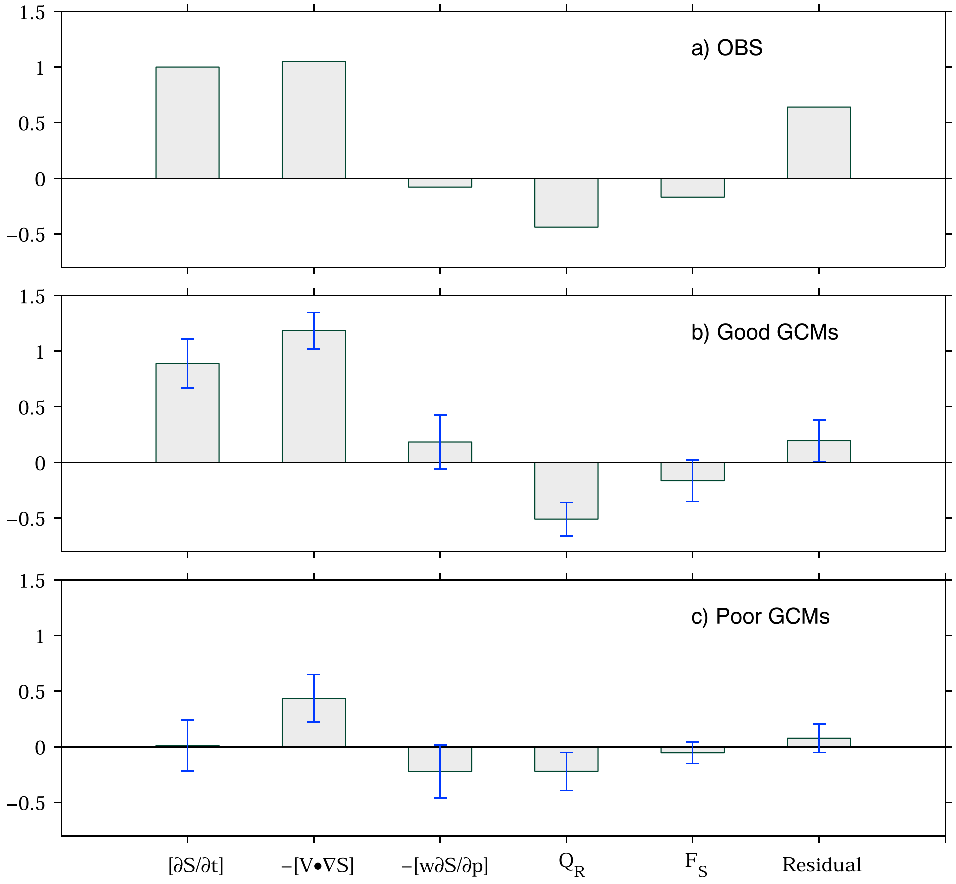

Figure 6. Relative role of each ME component for eastward propagation of the MJO by projecting spatial pattern of each vertically integrated ME budget term over the IO (50–110°E, 10°S–10°N) onto the corresponding observed pattern (Figure 3g) for (a) observations, composites based on (b) good and (c) poor MJO models. Error bars in Figures 6b and 6c denote spreads among six model members depicted by one standard deviation of projection coefficients.

also plays a negative role for the eastward propagation of convection in poor GCMs, largely due to the positive ME tendencies over the western IO as discussed in Figure 5f. While horizontal ME advection also exhibits a positive projection in poor GCMs, its magnitude is much weaker compared to that in the observations and good GCMs. As a result, the positive contribution for the eastward propagation by horizontal ME advection is largely offset by the three negative processes, leading to an overly stationary MJO mode in poor GCMs. Also worth mentioning is that relatively smaller projection residuals are noted in both good and poor model composites, which lend confidence to these above findings from ME budget analyses.

In summary, the above ME analyses suggest that horizontal ME advection plays a critical role for the eastward propagation of MJO convection in both observations and good GCMs, by generating an east-west dipole pattern in ME tendencies, namely, with positive (negative) ME tendencies to the east (west) of MJO convection center. The contribution by horizontal ME advection, however, is substantially underestimated in poor models and is largely offset by negative effects due to radiation, surface heat fluxes, and the vertical ME advection, leading to a stationary MJO mode in those model simulations.

4.3. Model Deficiencies in Simulating the Horizontal ME Advection Associated With the MJO

In order to further identify specific model processes responsible for underestimation in horizontal ME advection in poor model simulations, both horizontal winds and ME are decomposed into three different time scales when calculating the total vertically integrated horizontal ME advection, i.e., low-frequency (period $>$ 100 day, with mean seasonal cycle included), intraseasonal (MJO) (20–100 days), and high-frequency ($<$20 days) time scales. As a result, the total column horizontal ME advection consists of nine components with a combination of three different time scales in winds and ME. Contribution from each of these nine horizontal

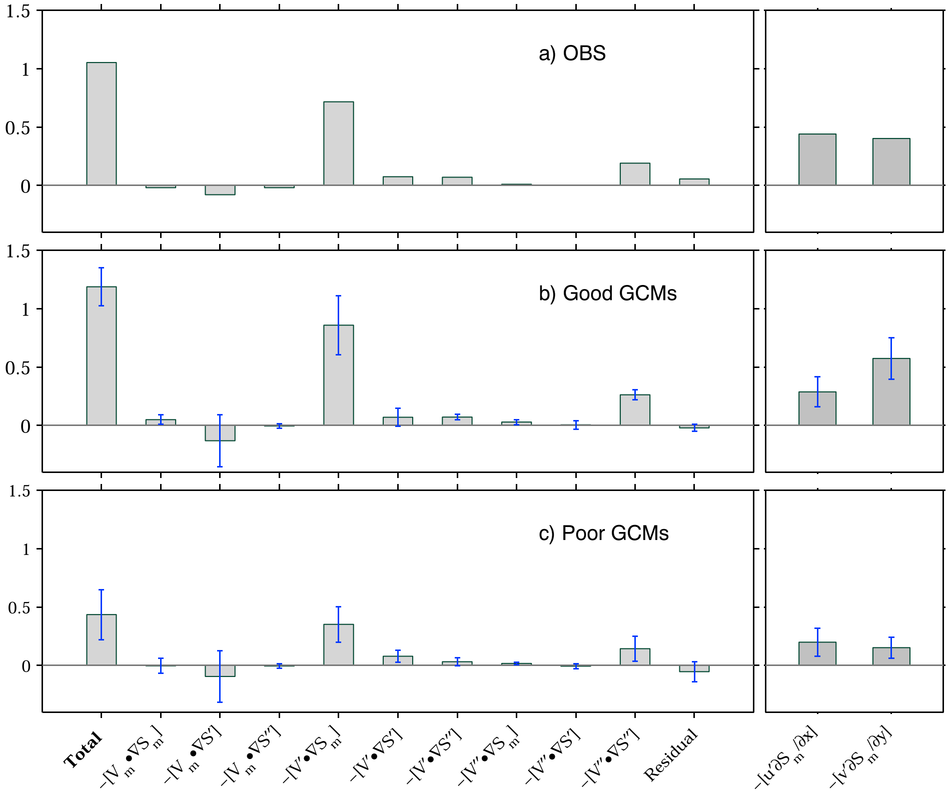

Figure 7. (left) Decomposition of the total horizontal ME advection by three different time-scales, i.e., low-frequency variability with period greater than 100 days (denoted by subscript "m"), MJO time-scale with a period between 20 and 100 days (denoted by a prime), and high-frequency variability (denoted by a double prime) in (a) observations, (b) good and (c) poor model simulations. (right) Decomposition of $\left[-\overrightarrow{v}'\cdot\nabla S_m\right]$ by zonal and meridional components. Error bars in Figures 7b and 7c denote spreads among six model members depicted by one standard deviation of projection coefficients.

ME advection components for the eastward propagation of the MJO can be similarly assessed by projecting their corresponding spatial patterns associated with the MJO, derived by lag-0 regression to rainfall at the IO base point, onto the observed total ME tendency pattern. For comparison purpose, temporal decomposition of the total column-integrated horizontal ME advection term is applied for both the observations and good versus poor model simulations, and results are presented in Figures 7a–7c (left). Since scale decomposition, regression, and projection are largely linear processes, the sum of the nine projection coefficients largely reproduces the projection coefficient of the total horizontal advection (see projection residuals in Figure 7).

Projections of the total horizontal ME advection are largely contributed by two major components, i.e., the low-frequency ME advection by the MJO winds $\left[-\overrightarrow{v}'\cdot\nabla S_m\right]$ and the high-frequency eddy ME transport $\left[-\overrightarrow{v}''\cdot\nabla S''\right]$ in both observations and model simulations. While role of MSE transport by high-frequency eddies for the eastward propagation of the MJO has been noted in previous observational and modeling studies [e.g., *Maloney*, 2009; *Kiranmayi and Maloney*, 2011; *Andersen and Kuang*, 2012; *Benedict et al.*, 2015], its amplitude is much weaker than the $\left[-\overrightarrow{v}'\cdot\nabla S_m\right]$ term, particularly in the observations and good GCMs (Figures 7a and 7b). The discrepancy regarding the role of high-frequency eddies for the total horizontal ME advection associated with the MJO between this study and previous studies could be largely due to different regions of analysis. While the ME budget analysis is conducted over the IO region in this study, more active role of high-frequency eddies for horizontal MSE advection is found over the western Pacific [e.g., *Maloney*, 2009; *Benedict et al.*, 2015]. A much weaker projection of the total vertically integrated horizontal ME advection in poor MJO GCMs as previously discussed is mainly due to a rather weak projection of the $\left[-\overrightarrow{v}'\cdot\nabla S_m\right]$ term (Figure 7c). Further decomposition of the total $\left[-\overrightarrow{v}'\cdot\nabla S_m\right]$ term into zonal $\left[-u'\frac{\partial S_m}{\partial x}\right]$ and meridional $\left[-v'\frac{\partial S_m}{\partial y}\right]$ components

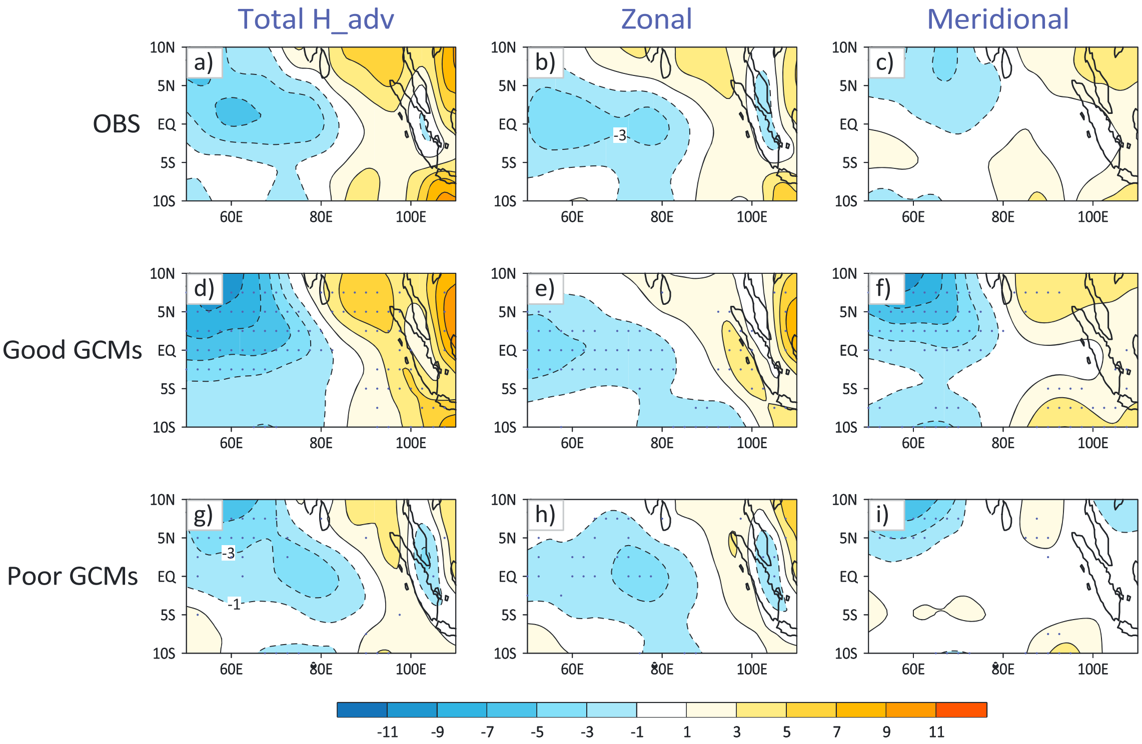

Figure 8. Same as in Figure 5 but for lag-0 regressed patterns for (a, d, and g) $\left[-\vec{v}'\cdot\nabla S_m\right]$ along with (b, e, and h) zonal and (c, f, and i) meridional components in observations (Figures 8a–8c), composites for good (Figures 8d–8f) and poor (Figures 8g–8i) MJO models. Units are W m^{-2}. Regions with model composite anomalies surpassing 95% significance level are stippled.

(Figures 7a–7c, right) suggests comparable contributions by both components in the observations, but a notable overestimated meridional component while reduced zonal component in good model simulations. In poor GCMs, both zonal and meridional components of $\left[-\vec{v}'\cdot\nabla S_m\right]$ are significantly underestimated, particularly the meridional component, leading to a substantially weak projection by the total $\left[-\vec{v}'\cdot\nabla S_m\right]$ term.

Figure 8 further illustrates spatial patterns of $\left[-\vec{v}'\cdot\nabla S_m\right]$ with its zonal and meridional components over the IO in both observations and simulations from the two model groups. A zonal dipole structure in the total $\left[-\vec{v}'\cdot\nabla S_m\right]$ pattern can be readily discerned in the observations (Figure 8a) and good model simulations (Figure 8d), resembling their corresponding total ME tendency patterns (Figures 3g and 3h), thus is consistent with their high projections onto the observed ME tendency. While the zonal advection is largely confined over the equatorial region (Figures 8b and 8e), particularly to the west of the convection center, the meridional advection is mainly characterized by off-equatorial maxima on both sides of the equator (Figures 8c and 8f). The overestimated meridional advection in good GCM simulations as previously mentioned is again readily discerned (cf. Figures 8c and 8f). For the total $\left[-\vec{v}'\cdot\nabla S_m\right]$ pattern in the poor GCMs (Figure 8g), an eastward shifted negative center toward the MJO center around 80°E is noted, along with much weaker positive tendencies to the east of convection center, both of which leading to a much weaker projection of $\left[-\vec{v}'\cdot\nabla S_m\right]$ as shown in Figure 7c. Decomposition of the total $\left[-\vec{v}'\cdot\nabla S_m\right]$ further suggests model deficiencies in both zonal and meridional advection components in poor model simulations, e.g., too weak negative zonal advection over the western IO (Figure 8h) and lack of positive off-equatorial tendencies to the east of convection by meridional advection (Figure 8i).

Since patterns of $\left[-\vec{v}'\cdot\nabla S_m\right]$ shown in Figure 8 have been subject to vertical integrations between 1000 hPa and 100 hPa, to further illustrate relative contributions from different vertical levels, longitude-pressure cross sections of $-\overrightarrow{V}' \cdot \nabla S_m$ fields averaged over 10°S–10°N are further illustrated in Figure 9 for both observations and model simulations. The strongest amplitudes of $-\overrightarrow{V}' \cdot \nabla S_m$ are discerned in the lower troposphere between 400 and 800 hPa in both observations (Figure 9a) and good MJO models (Figure 9b), with positive (negative) advection to the east (west) of the convection center near 80°E. The vertical profile of $-\overrightarrow{V}' \cdot \nabla S_m$ in poor GCMs, however, exhibits very different structure (Figure 9c), with strongest advection present below 800 hPa instead of the lower troposphere as in the observations and good GCM simulations.

Since column $\left[-\overrightarrow{V}' \cdot \nabla S_m\right]$ is primarily contributed by the lower troposphere in both the observations and good model simulations, Figure 10 displays anomalous MJO winds ($-\overrightarrow{V}'$) and winter mean ME (S_m) patterns at 600 hPa to further illustrate model deficiencies in the poor MJO models. The observed winter mean ME pattern at 600 hPa is characterized by a maximum over the Maritime Continent region (Figure 10a), decreasing both westward and poleward. Meanwhile, the observed anomalous MJO circulation at 600 hPa in corresponding to enhanced convection over the equatorial IO (80°E) is noted as a typical Gill-type responses [*Gill*, 1980], with Kelvin (Rossby) wave component to the east (west) of convection center. As a result, to the east of convection, advection of seasonal mean ME by both anomalous easterly zonal wind near the equator and slightly poleward off-equatorial meridional wind produces positive ME tendencies. Meanwhile, to the west of convection, advection of seasonal mean ME by both westerly wind anomalies near the equator and equatorward meridional winds particularly from the north generates strong negative ME tendencies, leading to the east-west dipole in the $-\overrightarrow{V}' \cdot \nabla S_m$ pattern (Figure 8a). In good model simulations, the maximum seasonal mean ME over the Maritime Continent is also discerned but with a weaker amplitude (Figure 10b), leading to a reduced zonal S_m gradient along the equator compared to the observations, albeit the meridional S_m gradient remains largely comparable to the observed. Meanwhile, the Gill-type wind anomalies at 600 hPa is well captured in good model simulations, but with a stronger amplitude than that in the observations. Thus, the weaker zonal S_m gradient but stronger MJO anomalous winds leads to underestimated zonal advection while overestimated meridional advection of seasonal mean ME in good MJO models as discussed in Figures 7 and 8. The total $-\left[\overrightarrow{V}' \cdot \nabla S_m\right]$ in good model composite, however, is largely comparable to its observed counterpart (Figure 9).

In poor GCM simulations, the horizontal gradient of S_m, particularly its zonal component, is substantially underestimated (Figure 10c). Moreover, corresponding to a much smaller convection size in poor MJO models (Figure 3c), wind anomalies also exhibit a smaller size in organization. Anomalous circulation is mainly confined in the Rossby wave part to the west of the convection center between 60 and 80°E. Meanwhile, the equatorial easterlies associated with Kelvin wave responses to the east of convection are rather weaker than the observations and good model simulations. Much weaker Kelvin wave responses in poor MJO models have also been noted at 850 hPa [*Jiang et al*., 2015]. As a result, significant deficiencies in simulating the vertically integrated $-\overrightarrow{V}' \cdot \nabla S_m$ pattern in poor MJO models are ascribed to model deficiencies in representing both the seasonal mean ME and anomalous circulation patterns in the lower troposphere.

5. Summary and Discussions

As a prominent climate variability mode with widespread influences on global weather and climate systems, the MJO remains poorly represented in the latest generation of GCMs, with a particular challenge in simulating its eastward propagating convective signals. Meanwhile, there is a lack of consensus on essential physics for the observed MJO propagation. In this study, by analyzing 24 model simulations from the recent MJOTF/GASS global model evaluation project, we make an effort to identify key processes for the eastward propagation of the MJO.

The basis of the analyses in this study is built upon the moisture mode framework for the MJO under a weak-temperature-gradient condition, in which evolution of the MJO convection is primarily regulated by moisture anomalies, which can be further linked to anomalous moist static energy (MSE). By employing an alternate form of the conventional MSE, i.e., moist entropy (ME), as a proxy of MJO convection, critical processes determining the eastward propagation of the MJO are investigated through comparison of simulations from two model groups, i.e., good versus poor MJO models, defined by their skill for the eastward propagation of

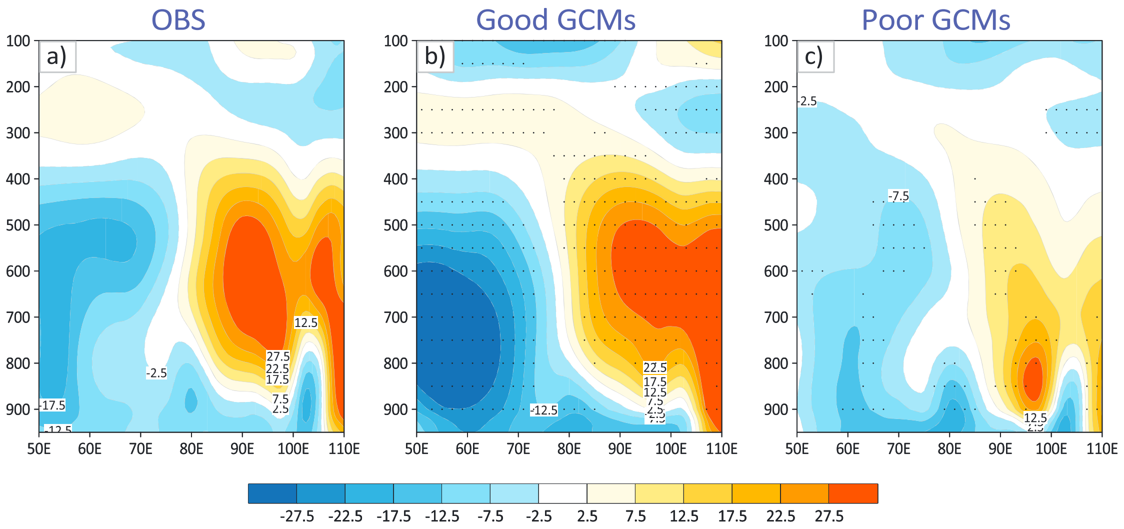

Figure 9. Longitude-pressure cross-section profiles of $-\overrightarrow{V}' \cdot S_m$ (units: 10^2 J m kg^{-1} s^{-1}) in (a) observations, (b) good and (c) poor MJO model composites, derived by lag-0 regressions to a 3 mm d^{-1} rainfall over the IO base point. All plots are based on an average between 10°S–10°N. Grid points with model composite anomalies surpassing 95% significance level are stippled.

MJO convection. Considering that the strongest eastward propagation of the MJO occurs over the Indian Ocean (IO), also to avoid complex influences on the MJO propagation by the Maritime Continent, we confine our analyses over the IO sector during the boreal winter season.

As predicted by the moisture mode theory, a close association between intraseasonal rainfall and ME anomalies, including their spatial patterns (Figure 3) and eastward propagation (Figures 1 and 2), is indeed discerned based on both observations and model simulations. In accord with evolution of convection signals, the eastward propagation of ME anomalies is clearly evident in the observations and good MJO models, while is absent in poor GCMs. Model fidelity in representing the observed ME tendency pattern over the IO is further found to be highly correlated to model skill for the eastward propagation of the MJO across these model simulations (Figure 4). These results lend support to the moisture mode theory for the MJO and provide a critical justification for using the ME analysis approach for understanding key physics for the eastward propagation of the MJO convection.

Relative roles of ME tendency terms in both observations and model simulations for the eastward propagation of the MJO are objectively assessed by projecting their spatial patterns to the observed ME tendency over the IO. While radiative effects and surface heat fluxes tend to inhibit the eastward propagation of the MJO as noted in previous studies, a determining factor for the eastward propagation of ME in observations and good models is found through the vertically integrated horizontal ME advection (Figure 6). In contrast to strong projections of column horizontal ME advection patterns onto the observed ME tendency in both observations and good GCMs, the projection is much weaker in poor model simulations. A weaker contribution for the eastward propagation by the horizontal ME advection is thus offset by negative effects from radiation and surface fluxes, leading to a largely stationary intraseasonal mode in the poor MJO GCMs.

Further analysis indicates that the vertically integrated horizontal ME advection in the observations and good model simulations is mainly through the advection of seasonal mean ME by MJO wind anomalies in the lower troposphere between 800 hPa and 400 hPa (Figures 7 and 9). With its maximum center situated over the Maritime Continent region, the observed winter mean lower tropospheric ME is characterized by a strong horizontal gradient in the IO, decreasing both westward and poleward. Meanwhile, low-level wind anomalies associated with enhanced MJO convection in the IO exhibit a typical Gill-type Kelvin-Rossby wave pattern (Figure 10a), producing positive (negative) ME advection to the east (west) of convention center (Figure 8a). The observed horizontal ME advection pattern is generally well simulated in the good MJO models, albeit through a trade-off between a weakened horizontal gradient of seasonal mean ME and an overestimated low-level MJO wind anomalies (Figure 10b). In the poor GCMs, the horizontal gradient of seasonal mean ME is significantly underestimated; meanwhile, the MJO convection and its associated circulation exhibit a much smaller scale in organization, with a particularly weak Kelvin-wave component to the east of convection (Figure 10c). As a result, the effect of the horizontal ME advection for the eastward propagation is substantially weaker than the observed, giving rise to a stationary MJO mode in the poor GCMs.

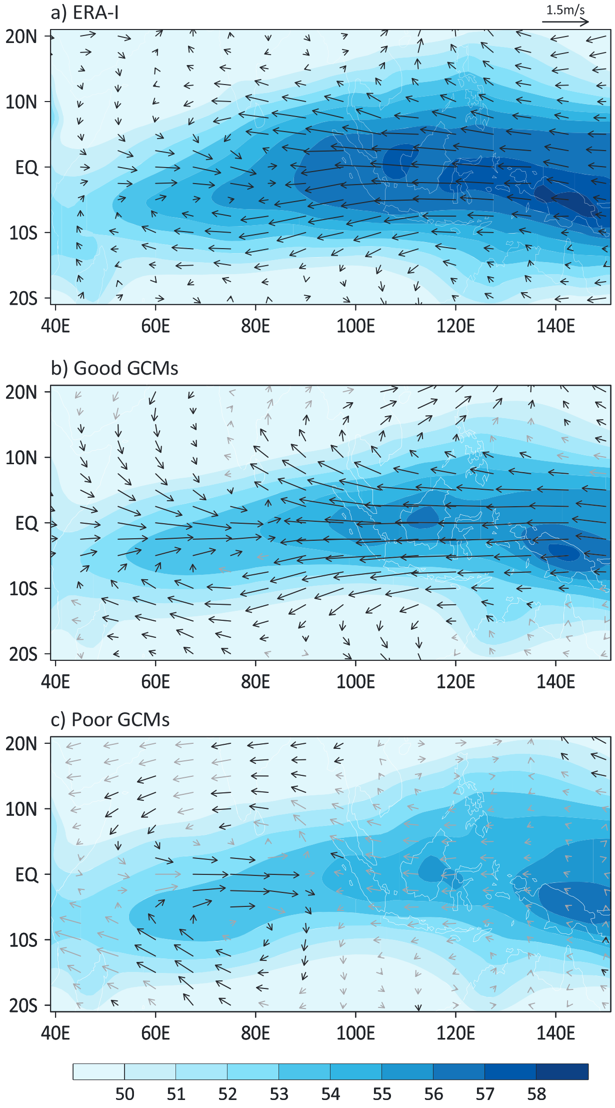

Figure 10. Winter (November–April) mean ME (shading; units: 10^3 J kg^{-1}) and MJO wind anomalies (vectors; see a scale on the top right) at 600 hPa, normalized by a 3 mm d^{-1} rainfall over the IO (75–85°E, 5°S–5°N) in (a) observations, (b) good versus (c) poor MJO models. Regions where either model composite *u* or *v* wind anomalies are significant at 95% significance level are denoted by black vectors.

Results from this study indicate that realistic representation of the lower tropospheric seasonal mean ME pattern and anomalous MJO circulations are critical for successfully simulating the eastward propagation of the MJO convection. Note that simulated anomalous MJO winds are further linked to model depiction of 3-D structure of the MJO convection, which could involve fundamental physics in regulating convective organization that remains poorly understood [e.g., *Held et al.*, 1993; *Emanuel et al.*, 2014]. Sensitivity tests by switching MJO anomalous winds and seasonal mean ME patterns between good and poor model composites suggest that model deficiencies in the seasonal mean ME pattern exert a stronger influence on the vertically integrated horizontal ME advection, thus the eastward propagation of the MJO. A close relationship between model skill for the lower tropospheric seasonal mean ME pattern over the Indo-Pacific region and model MJO skill in depicting its eastward propagation is indeed established based on these multimodel simulations, which will be reported in a separate manuscript. Therefore, the lower tropospheric mean ME pattern over the Indo-Pacific region, or equivalently the mean moisture pattern, can serve as an important diagnostic metric for the eastward propagation of the MJO in climate model simulations. However, since this study mainly focuses on impact of large-scale mean ME (moisture) pattern on the MJO propagation, one cannot exclude the possibility that the realistic lower tropospheric ME (moisture) in good MJO models is at least partially benefited from its realistic simulations of MJO activity. Upscale impact of the MJO on the mean ME (moisture) distribution over the Indo-Pacific region needs to be further investigated.

Note that in addition to the horizontal ME advections, the column-integrated vertical ME advection also plays a role in generating the east-west asymmetry in ME tendency in good MJO models, thus contributing to the eastward propagation of the convection. However, amplitude of the vertical ME advection is much weaker compared to its horizontal counterpart. Meanwhile, a near-zero projection of the vertical ME advection on the observed ME tendency is found in the observations. While the critical role of horizontal ME advection for the eastward propagation of the MJO is underscored in this study, worth mentioning is that results in this study are obtained with a particular focus on the MJO propagation over the IO with an attempt to expose fundamental model deficiencies in representing the eastward propagation of the MJO in the poor GCMs. Complex influences of the Maritime Continent on the MJO eastward propagation have been previously discussed [e.g., *Peatman et al*., 2014; *Kim et al*., 2014; *Feng et al*., 2015] and will be a main focus of the forthcoming "Year of the Maritime Continent" field campaign, which are beyond the scope of this study. On the other hand, while the horizontal ME advection mechanism could also be applied to interpret the MJO propagation over the western Pacific, particularly to the west of the low-level seasonal mean ME maximum (i.e., between 140 and 150°E; see Figure 10), detailed physics for the MJO propagation over the western Pacific could differ from that over the IO considering notable differences in mean states, including changes of horizontal gradient of the mean ME and the low-level zonal mean wind, as well as vertical tilting structure of the MJO from the IO to the western Pacific [*Jiang et al*., 2011]. Additionally, as previously discussed, meridional ME transport by high-frequency eddies could also play a more important role for the MJO propagation in the western Pacific [*Maloney*, 2009; *Benedict et al*., 2015]. All these factors could affect the MJO ME processes over the western Pacific, including both the horizontal and vertical ME, as well as surface fluxes and radiative effects, which warrant further investigations in the future study.

Acknowledgments
We thank modeling groups for making available their model output through the MJOTF/GASS MJO project. The multimodel output collected by this project and analyzed in this study is available for free download from https://earthsystemcog.org/projects/gassyotc-mip/. We acknowledge the insightful comments from the Editor, C. Zhang, and two anonymous reviewers. The author is indebted to E. Maloney, M. Zhao, D. Waliser, B. Wang, M. Pritchard, and WGNE MJO Task Force members for stimulating discussions during the course of this study. X. Jiang acknowledges support by the National Science Foundation (NSF) Climate and Large-Scale Dynamics Program under award AGS-1228302 and NOAA Climate Program Office MAPP program under awards NA12OAR4310075, NA15OAR4310098, and CVP program under award NA15OAR4310177.

References

Adames, Á. F., and D. Kim (2016), The MJO as a dispersive, convectively coupled moisture wave: Theory and observations, *J. Atmos. Sci.*, *73*, 913–941, doi:10.1175/JAS-D-15-0170.1.

Andersen, J. A., and Z. Kuang (2012), Moist static energy budget of MJO-like disturbances in the atmosphere of a zonally symmetric aquaplanet, *J. Clim.*, *25*, 2782–2804, doi:10.1175/jcli-d-11-00168.1.

Benedict, J. J., E. D. Maloney, A. H. Sobel, and D. M. W. Frierson (2014), Gross moist stability and MJO simulation skill in three full-physics GCMs, *J. Atmos. Sci.*, *71*, 3327–3349, doi:10.1175/JAS-D-13-0240.1.

Benedict, J. J., M. S. Pritchard, and W. D. Collins (2015), Sensitivity of MJO propagation to a robust positive Indian Ocean dipole event in the superparameterized CAM, *J. Adv. Model. Earth Syst.*, *7*, 1901–1917, doi:10.1002/2015MS000530.

Brown, A., S. Milton, M. Cullen, B. Golding, J. Mitchell, and A. Shelly (2012), Unified modeling and prediction of weather and climate: A 25-year journey, *Bull. Am. Meteorol. Soc.*, *93*, 1865–1877, doi:10.1175/BAMS-D-12-00018.1.

Dee, D. P., et al. (2011), The ERA-Interim reanalysis: Configuration and performance of the data assimilation system, *Q. J. R. Meteorol. Soc.*, *137*, 553–597, doi:10.1002/qj.828.

Duchon, C. E. (1979), Lanczos filtering in one and two dimensions, *J. Appl. Meteorol.*, *18*, 1016–1022.

Emanuel, K., A. A. Wing, and E. M. Vincent (2014), Radiative-convective instability, *J. Adv. Model. Earth Syst.*, *6*, 75–90, doi:10.1002/2013MS000270.

Feng, J., T. Li, and W. Zhu (2015), Propagating and nonpropagating MJO events over Maritime Continent, *J. Clim.*, *28*, 8430–8449, doi:10.1175/JCLI-D-15-0085.1.

Gill, A. E. (1980), Some simple solutions for heat-induced tropical circulation, *Q. J. R. Meteorol. Soc.*, *106*, 447–462.

Hagos, S. M., C. Zhang, Z. Feng, C. D. Burleyson, C. De Mott, B. Kerns, J. J. Benedict, and M. N. Martini (2016), The impact of the diurnal cycle on the propagation of Madden-Julian Oscillation convection across the Maritime Continent, *J. Adv. Model. Earth Syst.*, doi:10.1002/2016MS000725.

Held, I. M., R. S. Hemler, and V. Ramaswamy (1993), Radiative-convective equilibrium with explicit two-dimensional moist convection, *J. Atmos. Sci.*, *50*, 3909–3927, doi:10.1175/1520-0469(1993)050<3909:RCEWET>2.0.CO;2.

Hoskins, B. (2013), The potential for skill across the range of the seamless weather-climate prediction problem: A stimulus for our science, *Q. J. R. Meteorol. Soc.*, *139*, 573–584, doi:10.1002/qj.1991.

Huffman, G. J., R. F. Adler, D. T. Bolvin, G. Gu, E. J. Nelkin, K. P. Bowman, Y. Hong, E. F. Stocker, and D. B. Wolff (2007), The TRMM Multisatellite Precipitation Analysis (TMPA): Quasi-global, multiyear, combined-sensor precipitation estimates at fine scales, *J. Hydrometeorol.*, *8*, 38–55.

Hung, M.-P., J.-L. Lin, W. Wang, D. Kim, T. Shinoda, and S. J. Weaver (2013), MJO and convectively coupled equatorial waves simulated by CMIP5 climate models, *J. Clim.*, *26*, 6185–6214, doi:10.1175/JCLI-D-12-00541.1.

Hurrell, J., G. A. Meehl, D. Bader, T. L. Delworth, B. Kirtman, and B. Wielicki (2009), A unified modeling approach to climate system prediction, *Bull. Am. Meteorol. Soc.*, *90*, 1819–1832, doi:10.1175/2009BAMS2752.1.

Inoue, K., and L. Back (2015), Column-integrated moist static energy budget analysis on various time scales during TOGA COARE, *J. Atmos. Sci.*, *72*, 1856–1871, doi:10.1175/JAS-D-14-0249.1.

Jiang, X., D. E. Waliser, W. S. Olson, W.-K. Tao, T. S. L'Ecuyer, K.-F. Li, Y. L. Yung, S. Shige, S. Lang, and Y. N. Takayabu (2011), Vertical diabatic heating structure of the MJO: Intercomparison between recent reanalyses and TRMM estimates, *Mon. Weather Rev.*, *139*, 3208–3223, doi:10.1175/2011mwr3636.1.

Jiang, X., et al. (2015), Vertical structure and physical processes of the Madden-Julian oscillation: Exploring key model physics in climate simulations, *J. Geophys. Res. Atmos.*, *120*, 4718–4748, doi:10.1002/2014JD022375.

Jiang, X., M. Zhao, E. D. Maloney, and D. E. Waliser (2016), Convective moisture adjustment time scale as a key factor in regulating model amplitude of the Madden-Julian Oscillation, *Geophys. Res. Lett.*, *43*, 10,412–410,419, doi:10.1002/2016GL070898.

Kim, D., J.-S. Kug, and A. H. Sobel (2014), Propagating versus nonpropagating Madden–Julian Oscillation events, *J. Clim.*, *27*, 111–125, doi:10.1175/JCLI-D-13-00084.1.

Kiranmayi, L., and E. D. Maloney (2011), Intraseasonal moist static energy budget in reanalysis data, *J. Geophys. Res.*, *116*, D21117, doi:10.1029/2011JD016031.

Klingaman, N. P., X. Jiang, P. K. Xavier, J. Petch, D. Waliser, and S. J. Woolnough (2015a), Vertical structure and physical processes of the Madden-Julian oscillation: Synthesis and summary, *J. Geophys. Res. Atmos.*, *120*, 4671–4689, doi:10.1002/2015JD023196.

Klingaman, N. P., et al. (2015b), Vertical structure and physical processes of the Madden-Julian oscillation: Linking hindcast fidelity to simulated diabatic heating and moistening, *J. Geophys. Res. Atmos.*, *120*, 4690–4717, doi:10.1002/2014JD022374.

Lau, W. K.-M., and D. E. Waliser (2012), *Intraseasonal Variability in the Atmosphere-Ocean Climate System*, 2nd ed., p. 613, Springer, Heidelberg, Germany.

L'Ecuyer, T. S., and G. McGarragh (2010), A 10-year climatology of tropical radiative heating and its vertical structure from TRMM observations, *J. Clim.*, *23*, 519–541, doi:10.1175/2009jcli3018.1.

Lee, S.-S., B. Wang, D. Waliser, J. Neena, and J.-Y. Lee (2015), Predictability and prediction skill of the boreal summer intraseasonal oscillation in the Intraseasonal Variability Hindcast Experiment, *Clim. Dyn.*, *45*(7-8), 2123–2135, doi:10.1007/s00382-014-2461-5.

Madden, R. A., and P. R. Julian (1971), Detection of a 40–50 day oscillation in zonal wind in tropical Pacific, *J. Atmos. Sci.*, *28*, 702–708.

Madden, R. A., and P. R. Julian (1972), Description of global-scale circulation cells in tropics with a 40–50 day period, *J. Atmos. Sci.*, *29*, 1109–1123.

Maloney, E. D. (2009), The moist static energy budget of a composite tropical intraseasonal oscillation in a climate model, *J. Clim.*, *22*, 711–729.

Maloney, E. D., and A. H. Sobel (2004), Surface fluxes and ocean coupling in the tropical intraseasonal oscillation, *J. Clim.*, *17*, 4368–4386.

Mapes, B. E., and J. T. Bacmeister (2012), Diagnosis of tropical biases and the MJO from patterns in the MERRA analysis tendency fields, *J. Clim.*, *25*, 6202–6214, doi:10.1175/jcli-d-11-00424.1.

Moncrieff, M. W., D. E. Waliser, M. J. Miller, M. A. Shapiro, G. R. Asrar, and J. Caughey (2012), Multiscale convective organization and the YOTC virtual global field campaign, *Bull. Am. Meteorol. Soc.*, *93*, 1171–1187, doi:10.1175/bams-d-11-00233.1.

National Academies Press (2010), *Assessment of Intraseasonal to Interannual Climate Prediction and Predictability*, pp. 192, The National Academies Press, Washington, D. C.

National Academies Press (2016), *Next Generation Earth System Prediction: Strategies for Subseasonal to Seasonal Forecasts*, pp. 290, National Research Council, National Academy of Sciences, Washington, D. C.

Neale, R., and J. Slingo (2003), The Maritime Continent and its role in the global climate: A GCM study, *J. Clim.*, *16*, 834–848, doi:10.1175/1520-0442(2003)016<0834:TMCAIR>2.0.CO;2.

Neena, J. M., J. Y. Lee, D. Waliser, B. Wang, and X. Jiang (2014), Predictability of the Madden–Julian Oscillation in the Intraseasonal Variability Hindcast Experiment (ISVHE), *J. Clim.*, *27*, 4531–4543, doi:10.1175/JCLI-D-13-00624.1.

Peatman, S. C., A. J. Matthews, and D. P. Stevens (2014), Propagation of the Madden–Julian Oscillation through the Maritime Continent and scale interaction with the diurnal cycle of precipitation, *Q. J. R. Meteorol. Soc.*, *140*, 814–825, doi:10.1002/qj.2161.

Petch, J., D. Waliser, X. Jiang, P. Xavier, and S. Woolnough (2011), A global model inter-comparison of the physical processes associated with the MJO GEWEX News, August.

Pritchard, M. S., and C. S. Bretherton (2014), Causal evidence that rotational moisture advection is critical to the superparameterized Madden–Julian Oscillation, *J. Atmos. Sci.*, *71*, 800–815, doi:10.1175/JAS-D-13-0119.1.

Raymond, D. J. (2001), A new model of the Madden-Julian oscillation, *J. Atmos. Sci.*, *58*, 2807–2819.

Raymond, D. J. (2013), Sources and sinks of entropy in the atmosphere, *J. Adv. Model. Earth Syst.*, *5*, 755–763, doi:10.1002/jame.20050.

Raymond, D. J., and Ž. Fuchs (2009), Moisture modes and the Madden–Julian Oscillation, *J. Clim.*, *22*, 3031–3046, doi:10.1175/2008jcli2739.1.

Raymond, D. J., S. Sessions, A. Sobel, and Z. Fuchs (2009), The mechanics of gross moist stability, *J. Adv. Model. Earth Syst.*, *1*, 20, doi:10.3894/james.2009.1.9.

Reynolds, R. W., N. A. Rayner, T. M. Smith, D. C. Stokes, and W. Wang (2002), An improved in situ and satellite SST analysis for climate, *J. Clim.*, *15*, 1609–1625, doi:10.1175/1520-0442.

Sato, T., H. Miura, M. Satoh, Y. N. Takayabu, and Y. Wang (2009), Diurnal cycle of precipitation in the tropics simulated in a global cloud-resolving model, *J. Clim.*, *22*, 4809–4826, doi:10.1175/2009JCLI2890.1.

Serra, Y. L., X. Jiang, B. Tian, J. Amador Astua, E. D. Maloney, and G. N. Kiladis (2014), Tropical intra-seasonal modes of the atmosphere, *Annu. Rev. Environ. Resour.*, *39*, 189–215, doi:10.1146/annurev-environ-020413-134219.

Sobel, A., and E. Maloney (2012), An idealized semi-empirical framework for modeling the Madden–Julian Oscillation, *J. Atmos. Sci.*, *69*, 1691–1705, doi:10.1175/jas-d-11-0118.1.

Sobel, A., and E. Maloney (2013), Moisture modes and the eastward propagation of the MJO, *J. Atmos. Sci.*, *70*, 187–192, doi:10.1175/Jas-D-12-0189.1.

Sobel, A. H., J. Nilsson, and L. M. Polvani (2001), The weak temperature gradient approximation and balanced tropical moisture waves, *J. Atmos. Sci.*, *58*, 3650–3665.

Sobel, A. H., E. D. Maloney, G. Bellon, and D. M. Frierson (2008), The role of surface heat fluxes in tropical intraseasonal oscillations, *Nat. Geosci.*, *1*, 653–657, doi:10.1038/Ngeo312.

Sobel, A., S. Wang, and D. Kim (2014), Moist static energy budget of the MJO during DYNAMO, *J. Atmos. Sci.*, *71*, 4276–4291, doi:10.1175/JAS-D-14-0052.1.

Tian, B., D. E. Waliser, E. J. Fetzer, and Y. L. Yung (2010), Vertical moist thermodynamic structure of the Madden–Julian Oscillation in atmospheric infrared sounder retrievals: An update and a comparison to ECMWF Interim Re-Analysis, *Mon. Weather Rev.*, *138*, 4576–4582, doi:10.1175/2010MWR3486.1.

Vitart, F., et al. (2012), Subseasonal to seasonal prediction: Research implementation plan WWRP/THORPEX-WCRP Report.

Waliser, D. E. (2012), Predictability and Forecasting, in *Intraseasonal Variability in the Atmosphere-Ocean Climate System*, edited by W. K. M. Lau and D. E. Waliser, pp. 433–476, Springer, Heidelberg, Germany.

Waliser, D. E., et al. (2012), The "year" of tropical convection (May 2008–April 2010): Climate variability and weather highlights, *Bull. Am. Meteorol. Soc.*, *93*, 1189–1218, doi:10.1175/2011BAMS3095.1.

Wolding, B. O., E. D. Maloney, and M. Branson (2106), Vertically resolved weak temperature gradient analysis of the Madden-Julian Oscillation in SP-CESM, *J. Adv. Model. Earth Syst.*, doi:10.1002/2016MS000724.

Xavier, P. K., et al. (2015), Vertical structure and physical processes of the Madden-Julian Oscillation: Biases and uncertainties at short range, *J. Geophys. Res. Atmos.*, *120*, 4749–4763, doi:10.1002/2014JD022718.

Yoneyama, K., C. Zhang, and C. N. Long (2013), Tracking pulses of the Madden–Julian Oscillation, *Bull. Am. Meteorol. Soc.*, *94*, 1871–1891, doi:10.1175/BAMS-D-12-00157.1.

Yu, J. Y., and J. D. Neelin (1994), Modes of tropical variability under convective adjustment and the Madden-Julian Oscillation 2. Numerical results, *J. Atmos. Sci.*, *51*, 1895–1914.

Zhang, C. (2013), Madden–Julian Oscillation: Bridging weather and climate, *Bull. Am. Meteorol. Soc.*, *94*, 1849–1870, doi:10.1175/bams-d-12-00026.1.

Zhang, C. D. (2005), Madden-Julian Oscillation, *Rev. Geophys.*, *43*, RG2003, doi:10.1029/2004RG000158.

Zhang, C., J. Gottschalck, E. D. Maloney, M. W. Moncrieff, F. Vitart, D. E. Waliser, B. Wang, and M. C. Wheeler (2013), Cracking the MJO nut, *Geophys. Res. Lett.*, *40*, 1223–1230, doi:10.1002/grl.50244.